

Hypersoft X-ray Sources: A New Class of Luminous Cosmic Emitters

Mustafa Muhibullah^{1*}, Jimmy A. Irwin^{1†}, R. Di Stefano^{2†}

¹ Department of Physics and Astronomy, University of Alabama, Box 870324, Tuscaloosa, 35487, AL, USA.

² Center for Astrophysics, Harvard & Smithsonian, 60 Garden St., Cambridge, 02138, MA, USA.

* Corresponding author. Email: mmuhibullah@crimson.ua.edu;

† These authors contributed equally to this work.

X-ray binaries, powered by black holes, neutron stars, or white dwarfs accreting matter from a companion star, are among the brightest beacons in galaxies, outshining the Sun by a factor of millions. Most emit primarily above 0.3 keV in X-rays, but cooler thermal sources peaking in the extreme ultraviolet (EUV) would be much more difficult to detect due to astronomy's critical blind spot in EUV. Here, we report the discovery of a remarkable new class of luminous, point-like, non-nuclear X-ray objects in galaxies—hypersoft X-ray sources—that have been missed by all previous surveys to date. Detected primarily or exclusively below 0.3 keV, with 0.15–0.3 keV to 0.3–1.0 keV photon ratios $\gtrsim 8$, the most luminous examples radiate $\geq 10^{38}$ erg/s in the narrow X-ray band, with spectral models indicating even greater bolometric luminosities, largely emitted in the EUV. They rank among the most energetic sources in galaxies, yet their EUV-peaking spectra evaded earlier detections. We propose that hypersoft sources are X-ray binaries spanning multiple physical classes, including accreting white dwarfs or post-nova systems—potential Type Ia supernova progenitors—and systems hosting accreting black holes. Beyond their elusive nature, they may play crucial role in ionizing gas within galaxies¹.

The extreme ultraviolet (EUV) window, spanning 100–912 Å (13.6 eV–0.124 keV), occupies a critical yet largely uncharted territory of the electromagnetic spectrum². Despite its importance for understanding hot astrophysical sources, the neutral hydrogen and helium in the interstellar medium absorb EUV photons so efficiently that they form a nearly impenetrable barrier^{3,4}. While the EUV band remains largely inaccessible, EUV-peaking spectra would be expected to emit a detectable soft X-ray tail of emission that offers a potential indirect window into this hidden domain. Even so, detecting EUV-peaking sources via their soft X-ray tail is inherently challenging: lower-energy X-ray photons are also susceptible to extinction by Galactic gas, and most current X-ray detectors exhibit rapidly declining sensitivity below 0.5 keV.

We conducted a systematic search for extremely soft X-ray sources which could represent the high energy tail of a hidden EUV population of sources. We searched in six well-observed, nearby external galaxies using archival *Chandra* data. These galaxies were selected for their long exposure times, proximity, and diversity in galaxy type, optimizing the chances of uncovering these exceptionally soft X-ray emitters. By imposing stringent selection criteria, we uncovered a previously unrecognized population of sources that emit primarily or exclusively below 0.3 keV. We refer to these objects as hypersoft X-ray sources (HSSs)—a newly revealed class that radiates at the lowest energies accessible to modern X-ray instrumentation, making them among the softest X-ray sources yet observed. To identify HSSs, we required $\geq 3\sigma$ detections in the 0.15–0.3 keV energy range, with no significant emission above 0.3 keV. To ensure a more conservative classification, we impose an additional criterion that the photon ratio between the 0.15–0.3 keV and 0.3–1.0 keV bands must exceed ~ 8 (see *Methods*). For two galaxies, NGC 3379 and NGC 4472, Fig. 1 illustrates that the HSSs are bright below 0.3 keV but exhibit no emission above that value. This name is given to contrast them to the somewhat harder supersoft X-ray sources (SSSs)⁵,

which emit energies up to around 1.0 keV^{6,7}. Like HSSs, SSSs are phenomenologically defined by their ranges of temperatures and luminosities. The class includes black hole (BH) and white dwarf (WD) accretors, either actively accreting material from a companion star⁸, or in a post-nova phase with residual hydrogen shell burning⁹, and potentially neutron stars.

We discovered 84 HSSs, with 7 to 21 in each galaxy (Table 1), found in both star-forming and older galactic populations. While a few, nearby low luminosity HSSs were previously known X-ray sources, nearly all of the more luminous and distant HSSs remained undiscovered, despite decades of X-ray observations. This is because the current generation of X-ray telescopes either lack the spatial resolution or the collecting area below 0.3 keV to have readily detected these sources previously. Detectability of HSSs depends strongly on both source location and instrumental sensitivity; as a result, the number of detected HSSs likely represents a lower limit of the true underlying population within each host galaxy. A comprehensive list of source properties is provided in Extended Data Table 1.

HSSs are detected with 0.15–0.3 keV X-ray luminosities ranging from 10^{35} - 10^{38} erg/s, depending on the detection limits of each galaxy (see *Methods* for spectral fitting details). The lowest-luminosity HSSs are detectable only in our nearest galactic neighbor, M31. Sources with 10^{36} - 10^{37} erg/s can be found in M101, which is closer than the other galaxies on our list, and which has had a very deep (~1 megasecond) exposure. These galaxies are also the only spiral galaxies we have studied. Given the greater distances and relatively shorter exposures of the other galaxies on our list, which are early-type galaxies, only the brightest HSSs can be detected. Intriguingly, since the sources are peaking in the EUV, their total bolometric energy output must be markedly higher than these limited bandwidth values.

Although precise temperature measurements are limited by low count rates and calibration uncertainties below 0.3 keV in *Chandra*, the complete lack of significant emission in the harder 0.3–1.0 keV band strongly indicates that these sources have exceptionally low temperatures, likely not exceeding \sim 20 eV (230,000 K; see *Methods*). Supporting this estimate, two lower-luminosity sources in M31 have derived blackbody temperatures of 11 eV (130,000 K; M31N 2001-10a)¹⁰ and 17 eV (200,000 K; M31N 1996-08b)¹¹. Theoretically, a 20-eV blackbody spectrum implies a bolometric correction factor of \sim 18 to the 0.15–0.3 keV luminosity. This suggests that the most luminous HSSs found so far have bolometric luminosities of at least 1×10^{39} erg/s, and potentially considerably higher if their temperatures are below 20 eV, given the steep temperature dependence of the correction factor in the narrow 0.15–0.3 keV band (see Extended Data Fig. 2). Even without applying a bolometric correction, several HSSs already reach \sim 10³⁸ erg s⁻¹ in this band, including when the lower bounds of the measurement uncertainties are considered (see *Methods*). These results are supported by multiple independent approaches (see *Spectral Analysis* in *Methods*), and in fact, all plausible spectral models—not limited to thermal blackbodies—predict similarly high bolometric luminosities.

By comparison, known very soft Galactic sources such as AG Draconis (AG Dra)¹², which also emit predominantly below 0.3 keV, have much lower luminosities. The most luminous sources in NGC 4472 already reach \sim 10³⁸ erg s⁻¹ in the 0.15–0.3 keV band—an order of magnitude higher than AG Dra’s bolometric luminosity. This discrepancy is substantial even without a bolometric correction, and becomes more pronounced when accounting for the fact that any realistic spectral model—not only blackbodies—implies a large bolometric correction. For reference, AG Dra has a bolometric correction of order \sim 100, which raises its observed 0.15–0.3 keV luminosity from \sim 2 \times 10³⁵ erg s⁻¹ to a bolometric luminosity of \sim 1 \times 10³⁷ erg s⁻¹ (see *Methods*).

HSSs are clearly associated with the galaxies we are studying. In the elliptical galaxy NGC 3379, for instance, a substantial concentration of HSSs is observed near the galaxy's center (Fig. 1), where they account for at least 20% of the detected X-ray sources. In other elliptical or bulge-dominated galaxies, HSSs are often seen farther from the central region, yet generally remain confined within the halo. Meanwhile, in the spiral galaxy M101—the only surveyed galactic disk in our sample—HSSs primarily appear along the spiral arms (Fig. 2). The connection between the spatial distributions of HSSs and the galaxy morphologies rules out both a cosmological and a Milky Way origin, indicating that HSSs represent a distinct point-source population that urges a new classification. Furthermore, the absence of HSSs in deep *Chandra* observations of non-galaxy fields strengthens their galactic association. Their presence in the older stellar populations of elliptical galaxies and spiral bulges (e.g., M31) suggests that these sources are not exclusively linked to recent star formation.

Since many HSSs were only detected in merged *Chandra* observations covering many years, their time variability is difficult to assess. A few HSSs in NGC 3379 and M101 show intra-observation variability, while others remain detectable over timescales of about a year (when observed through individual exposures during that period). Intriguingly, some HSSs may completely turn off, as indicated by their absence in later observations (Fig. 3). It is also possible that some of these sources may cool to a level where they no longer emit enough 0.15–0.3 keV photons to be detected, thus only appearing to disappear. Whether HSSs are inherently persistent, transient, or recurrent remains uncertain, as their low count rates necessitate deep exposures for reliable detection. For most suitable targets—those that are nearby, large, low in hot gas content, and situated behind minimal Galactic absorption—only a single long *Chandra* observation is typically available for the entire *Chandra* mission. However, in NGC 4472, at least two HSSs

exhibit clear 0.15–0.3 keV emission over a span of 11 years (Fig. 4). Although neither source showed significant emission during the relatively shorter 2010 observation, both were detected in earlier (2000; ~40 ks) and later (2011; ~136 ks) observations, suggesting possible recurrence and even persistence.

Apart from several known sources in M31 associated with post-nova systems, only a small fraction of sources in other galaxies have detectable counterparts at other wavelengths. In NGC 3115, for example, we identified an HSS (HSS J100514.4–074358; Extended Data Table 1) that coincides with a point source in Hubble Space Telescope (HST) ACS/WFC F475W imaging from March 2012 (see *Methods*). The source was undetected in X-rays before February 2012, appeared in the optical in March 2012, and was again undetected in X-rays in April 2012; there is no useful UV coverage for this object. In M101, HSS J140300.4+541951 lies in a crowded HST WFC3/UVIS F300X field, with at least one UV source within the 1σ X-ray positional uncertainty. In NGC4472, we could associate just 2 of the 21 HSSs with globular clusters, in strong contrast to normal X-ray binaries, which have long been known to be over-represented in such star clusters (~10–70%) due to likely dynamical effects within the star clusters that are conducive to forming mass-transfer binary systems^{13–15}. Interestingly, an HSS in NGC 3379 (marked in yellow in Fig. 3) seems to have a UV counterpart (0.7'' offset) associated with a young star cluster from the 2009/10 HST observation¹⁶. The 0.15–0.3 keV light curve (yellow markers) reveals that the source was X-ray bright only during the 2006 epoch and disappeared in the most recent 2007 *Chandra* observation.

Overall, HSSs are generally not associated with galactic star clusters. However, it is important to note that most normal non-globular-cluster X-ray sources in external galaxies also lack detectable optical counterparts, so the absence of optical detections for most HSSs is not

unexpected. In particular, a WD with a low-mass companion would not be detectable at optical wavelengths at distances of ~ 10 Mpc. Moreover, for sources hotter than ≈ 18 eV, a thermal blackbody model predicts that the far-UV tail of the spectrum would fall below the detection limits of the existing HST data.

The physical nature (or natures) of HSSs remains unclear and are likely a heterogeneous mix. The term ‘hypersoft’ is purely phenomenological and may reflect an observational trait shared by multiple types of objects, rather than indicating a single, unified class. Unrelated sources may exhibit a ‘hypersoft state’ under different physical conditions. Many low-luminosity ($L_X < 10^{36}$ erg/s) HSSs in M31 are known post-nova systems (at least six) and were historically classified as SSSs, but during *Chandra* observations they emit almost exclusively below 0.3 keV. For example, HSS J004255.2+412046 ($kT \approx 17$ eV) is coincident (angular offset $\sim 0.8''$) with nova M31N 1996–08b¹⁰, which exhibits an unusually long soft X-ray phase, turning on ~ 1831 days and fading ~ 13.8 years after the optical outburst¹¹. Another source, HSS J004303.3+411212 ($kT \approx 11$ eV), coincides (offset $\sim 0.1''$) with Nova M31N 2001–10a, with soft X-ray emission from 1089 days to ~ 9.6 years post-outburst¹¹. Such systems appear as SSSs if the material ejected by the nova has become diffuse enough to allow soft X-rays to penetrate. This occurs during the interval when the post-nova WD ceases nuclear burning and begins to cool^{11,17}. As it continues to cool, a hypersoft state may be expected for some time. Indeed, we identified several sources that we classify as SSSs exhibiting such behavior. For example, in M31, an early SSS (CXOGSG J004232.6+411702) source was later observed as an HSS source.

Even more intriguing are the highest luminosity ($L_X \approx 10^{38}$ erg/s) sources seen in the large elliptical galaxies. With bolometric corrections, these sources are emitting at more than 10^{39} erg/s, as much total energy as ultraluminous X-ray sources (ULXs)^{18,19}, but exist at significantly larger

numbers per galaxy (at least 20) compared to ULXs (fewer than two per galaxy, depending on star formation rate)²⁰ and are not confined primarily to star-forming galaxies like ULXs. In galaxies lacking an active galactic nucleus (AGN) and star formation-induced ULXs, HSSs represent the most luminous point sources in those galaxies, and yet they remained undiscovered until now because of their extremely soft X-ray emission being missed by previous surveys.

It has been conjectured that WDs that accrete and burn matter undergo thermonuclear explosions as Type Ia supernovae (SNe Ia) when they achieve the Chandrasekhar mass^{21,22}. The discovery of SSSs, which have the high luminosities expected from nuclear burning, and effective radii comparable to WDs, suggested that they could be the long-sought progenitors⁸. Studies of external galaxies^{23,24} concluded that SSSs are not numerous enough by about 1–2 orders of magnitude to account for the observed SNe Ia rate in galaxies. Additional work on those SSSs that appear to be steady-nuclear burners showed that some exhibit X-ray off states consistent with the expansion of the photosphere and a shift of the emission to longer, EUV wavelengths²⁵. This model predicts the existence of bright HSSs, and indeed, at least one such shift has been observed from the SSS to the HSS regime in one source within NGC 4472. It may therefore be the case that nuclear-burning WDs manifest as both SSSs and HSSs.

Table 1 shows that adding HSSs increases the number of potential WD accretors by a factor of ~ 2 over previous estimates. Note in addition, that the detectable numbers of HSSs almost certainly represent only the tip of the population's iceberg since the EUV radiation they emit is readily absorbed. Similarly, detected SSSs constitute only a small fraction of their true populations, as the detectability of both populations is limited by observational constraints and the integrated effects of gas and dust along the line of sight^{8,26}. We therefore consider the possibility that these extremely luminous HSSs could represent a significant fraction of the missing progenitors of SNe

Ia. Together with the true SSS population, they may account for the total number needed to match the observed SNe Ia rate in galaxies. We note, however, that not all accreting WDs reaching the Chandrasekhar limit will necessarily produce SNe Ia, as only carbon–oxygen (CO) WDs can release sufficient nuclear energy to trigger such explosions. Since CO WDs generally form with lower masses than oxygen–neon (ONe) WDs, their growth to the Chandrasekhar mass in binary systems presents additional challenges, leaving the connection between nuclear-burning WDs and SN Ia progenitors an open question. Therefore, arguments against soft X-ray sources being the progenitors of supernovae need to be revisited given the discovery of HSSs.

Interestingly, for the highest-luminosity HSSs ($L_X \approx 10^{38}$ erg/s) with effective temperatures ~ 10 eV, the bolometric correction would raise the luminosity by several hundred times or more, resulting in a bolometric luminosity of $L_{\text{bol}} \geq 10^{40}$ erg/s. Even under the most conservative bolometric corrections, a luminosity of 10^{38} erg/s is difficult to reconcile with accreting WD models, as no WD has ever been observed to radiate at such extreme levels. This suggests the need for an alternative explanation, with an accreting BH as one possible candidate.

Regardless of their exact nature, the temperature ranges of HSSs suggest they could significantly contribute to ionizing large portions of the interstellar medium within galaxies. For decades, the detection of high-ionization emission lines, such as HeII (ionization energy of ~ 54 eV) in non-AGN star-forming galaxies has remained a puzzling mystery. Conventional photoionization models involving main-sequence and giant stellar populations fail to account for the HeII emission observed in both local and high-redshift galaxies. A recent study¹ proposed that soft X-ray sources such as SSSs might supply sufficient hard ionizing photons to produce these highly ionized lines. In some cases, thermal components between 5 and 20 eV were found necessary to match the observed HeII to the H β emission line ratios, indicating that HSSs could

be instrumental in interpreting the ionization signatures detected by SDSS and JWST in galaxies across both low²⁷ and high redshifts²⁸. The discovery of HSSs raises the intriguing possibility that this enigmatic class of sources may hold the key to two of astrophysics' long-standing puzzles—the origin of high-ionization lines in galaxies and the progenitors of SNe Ia.

References

1. Triani, D. P., Di Stefano, R. & Kewley, L. J. The significant contribution of supersoft X-ray Sources to the nebular HeII line emission. Preprint at <https://doi.org/10.48550/arXiv.2405.08121> (2024).
2. Drake, J. J., Kashyap, V. L., Wargelin, B. J. & Wolk, S. J. Pointing Chandra toward the Extreme Ultraviolet Fluxes of Very Low Mass Stars. *Astrophys. J.* **893**, 137 (2020).
3. McCammon, D. & Sanders, W. T. The soft X-ray background and its origins. *Annu. Rev. Astron. Astrophys.* **28**, 657–688 (1990).
4. Jelinsky, P., Vallerga, J. V. & Edelstein, J. First Spectral Observations of the Diffuse Background with the Extreme Ultraviolet Explorer. *Astrophys. J.* **442**, 653 (1995).
5. Kahabka, P. & Heuvel, E. P. J. van den. LUMINOUS SUPERSOFT X-RAY SOURCES. *Annu. Rev. Astron. Astrophys.* **35**, 69–100 (1997).
6. Greiner, J., Hasinger, G. & Kahabka, P. ROSAT observation of two supersoft sources in the Large Magellanic Cloud. *Astron. Astrophys.* **246**, L17–L20 (1991).
7. Trümper, J. *et al.* X-ray survey of the Large Magellanic Cloud by ROSAT. *Nature* **349**, 579–583 (1991).
8. Rappaport, S., Di Stefano, R. & Smith, J. D. Formation and Evolution of Luminous Supersoft X-Ray Sources. *Astrophys. J.* **426**, 692 (1994).

9. Orio, M., Covington, J. & Ögelman, H. X-ray emission from classical and recurrent novae observed with ROSAT. *Astron. Astrophys.* **373**, 542–554 (2001).
10. Henze, M. *et al.* X-ray monitoring of classical novae in the central region of M 31 - II. Autumn and winter 2007/2008 and 2008/2009. *Astron. Astrophys.* **533**, A52 (2011).
11. Henze, M. *et al.* X-ray monitoring of classical novae in the central region of M 31 III. Autumn and winter 2009/10, 2010/11, and 2011/12. *Astron. Astrophys.* **563**, A2 (2014).
12. González-Riestra, R. *et al.* AG Draconis observed with XMM-Newton. *Astron. Astrophys.* **481**, 725–734 (2008).
13. Fabbiano, G. Populations of X-Ray Sources in Galaxies. *Annu. Rev. Astron. Astrophys.* **44**, 323–366 (2006).
14. Paolillo, M. *et al.* Probing the GC-LMXB Connection in NGC 1399: A Wide-field Study with the Hubble Space Telescope and Chandra. *Astrophys. J.* **736**, 90 (2011).
15. Joseph, T. D., Maccarone, T. J., Kraft, R. P. & Sivakoff, G. R. A deeper look at the X-ray point source population of NGC 4472. *Mon. Not. R. Astron. Soc.* **470**, 4133–4144 (2017).
16. Ford, H. A. & Bregman, J. N. Direct detections of young stars in nearby elliptical galaxies. *Astrophys. J.* **770**, 137 (2013).
17. Pietsch, W. *et al.* Optical novae: the major class of supersoft X-ray sources in M 31. *Astron. Astrophys.* **442**, 879–894 (2005).
18. Avdan, H. & Avdan, S. Exploring the nature of an ultraluminous X-ray source in NGC 628. *Astron. Astrophys.* **690**, A335 (2024).
19. Panurach, T. *et al.* Do Neutron Star Ultraluminous X-Ray Sources Masquerade as Intermediate-mass Black Holes in Radio and X-Ray? *Astrophys. J.* **977**, 211 (2024).

20. Walton, D. J., Roberts, T. P., Mateos, S. & Heard, V. 2XMM ultraluminous X-ray source candidates in nearby galaxies. *Mon. Not. R. Astron. Soc.* **416**, 1844–1861 (2011).
21. Hoyle, F. & Fowler, W. A. Nucleosynthesis in Supernovae. *Astrophys. J.* **132**, 565 (1960).
22. Whelan, J. & Iben, I., Jr. Binaries and Supernovae of Type I. *Astrophys. J.* **186**, 1007–1014 (1973).
23. Di Stefano, R., Primini, F. A., Liu, J., Kong, A. & Patel, B. Populations of supersoft X-ray sources: Novae, tidal disruption, Type Ia supernovae, accretion-induced collapse, ionization, and intermediate-mass black holes? *Astronomische Nachrichten* **331**, 205–211 (2010).
24. Gilfanov, M. & Bogdán, Á. Progenitors of type Ia supernovae in elliptical galaxies. *AIP Conference Proceedings* **1379**, 17–22 (2011).
25. Greiner, J. & Di Stefano, R. X-ray off states and optical variability in CAL 83. *Astron. Astrophys.* **387**, 944–954 (2002).
26. Rappaport, S., Podsiadlowski, Ph., Joss, P. C., Di Stefano, R. & Han, Z. The relation between white dwarf mass and orbital period in wide binary radio pulsars. *Mon. Not. R. Astron. Soc.* **273**, 731–741 (1995).
27. Shirazi, M. & Brinchmann, J. Strongly star forming galaxies in the local Universe with nebular He iiλ4686 emission. *Mon. Not. R. Astron. Soc.* **421**, 1043–1063 (2012).
28. Heintz, K. E. *et al.* Strong damped Lyman- α absorption in young star-forming galaxies at redshifts 9 to 11. *Science* **384**, 890–894 (2024).

Table 1 | A summary of HSS/SSSs detected in six nearby galaxies.

Galaxy	Type	No. of Obs.	Total Exp. (ks)	D (Mpc)	N_{H} (10^{20}cm^{-2})	HSSs	SSSs	L_{X} (HSS) (erg/s)
M31 (bulge)	Sb	13	369	0.8	6.68	18	17	$10^{35}\text{-}10^{36}$
M101	SABc (face-on)	25	1057	6.5	1.15	7	53	$10^{36}\text{-}10^{37}$
NGC 3115	E-S0	11	1139	9.7	4.61	18	12	$10^{36}\text{-}10^{37}$
NGC 3379	E	5	337	10.6	2.79	12	18	$10^{36}\text{-}10^{37}$
NGC 4697	E	5	193	11.4	2.14	8	11	$10^{36}\text{-}10^{37}$
NGC 4472	E	10	476	16.7	1.62	21	21	$10^{37}\text{-}10^{38}$

Notes: (i) Morphological classification from the HyperLeda catalog³¹. (ii) The distances (D) are from³²⁻³⁷. (iii) N_{H} are estimated from published values of Galactic HI column densities³⁸. (iv) HSSs are defined as sources with no significant detection above 0.3 keV and a 0.15–0.3 keV to 0.3–1.0 keV photon ratio > 8 , whereas SSSs are defined as sources detected only at ≤ 1.0 keV with no emission at higher energies. (v) All L_{X} values correspond to the 0.15–0.3 keV energy range.

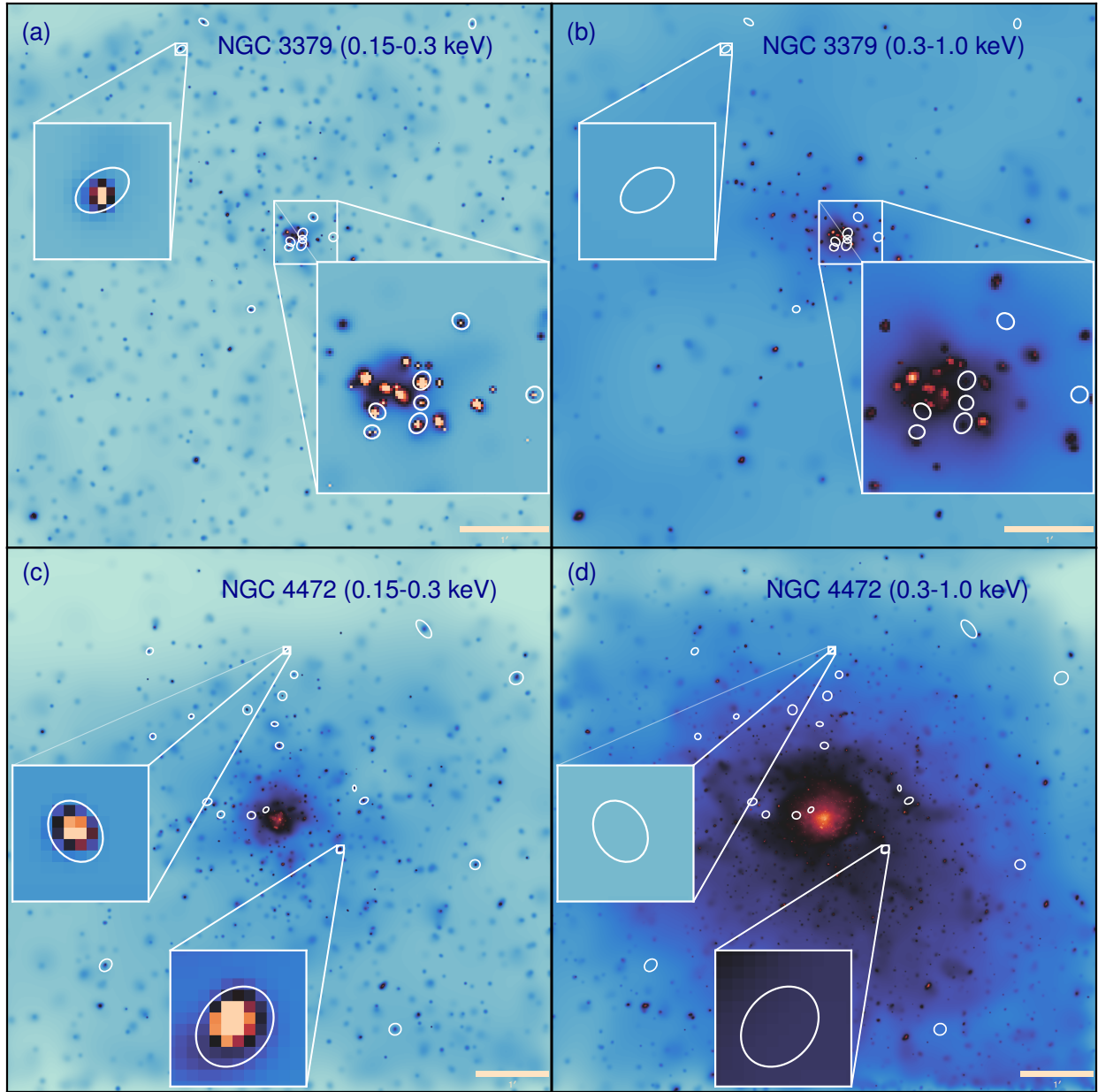


Figure 1 | Smoothed composite *Chandra* images of NGC 3379 and NGC 4472. (a-b) 0.15–0.3 keV and 0.3–1.0 keV band images of NGC 3379, respectively, combining 337 ks of observations. (c-d) 0.15–0.3 keV and 0.3–1.0 keV band images of NGC 4472, respectively, combining 476 ks of observations. The white ellipses, slightly enlarged for visual clarity, represent detections from the *Chandra* source detection tool `wavdetect`, which accounts for the point-spread function's size and orientation at each source location. They highlight the locations of the HSSs detected with at least 3σ significance in the 0.15–0.3 keV band but not above 0.3 keV. The insets show detections of HSSs that do not appear in the 0.3–1.0 keV bands. None of the HSSs appear in the *Chandra* Source Catalog version 2.1²⁹ or the comprehensive source list of^{15,30}, as most investigators tend to ignore energy channels below 0.3 keV.

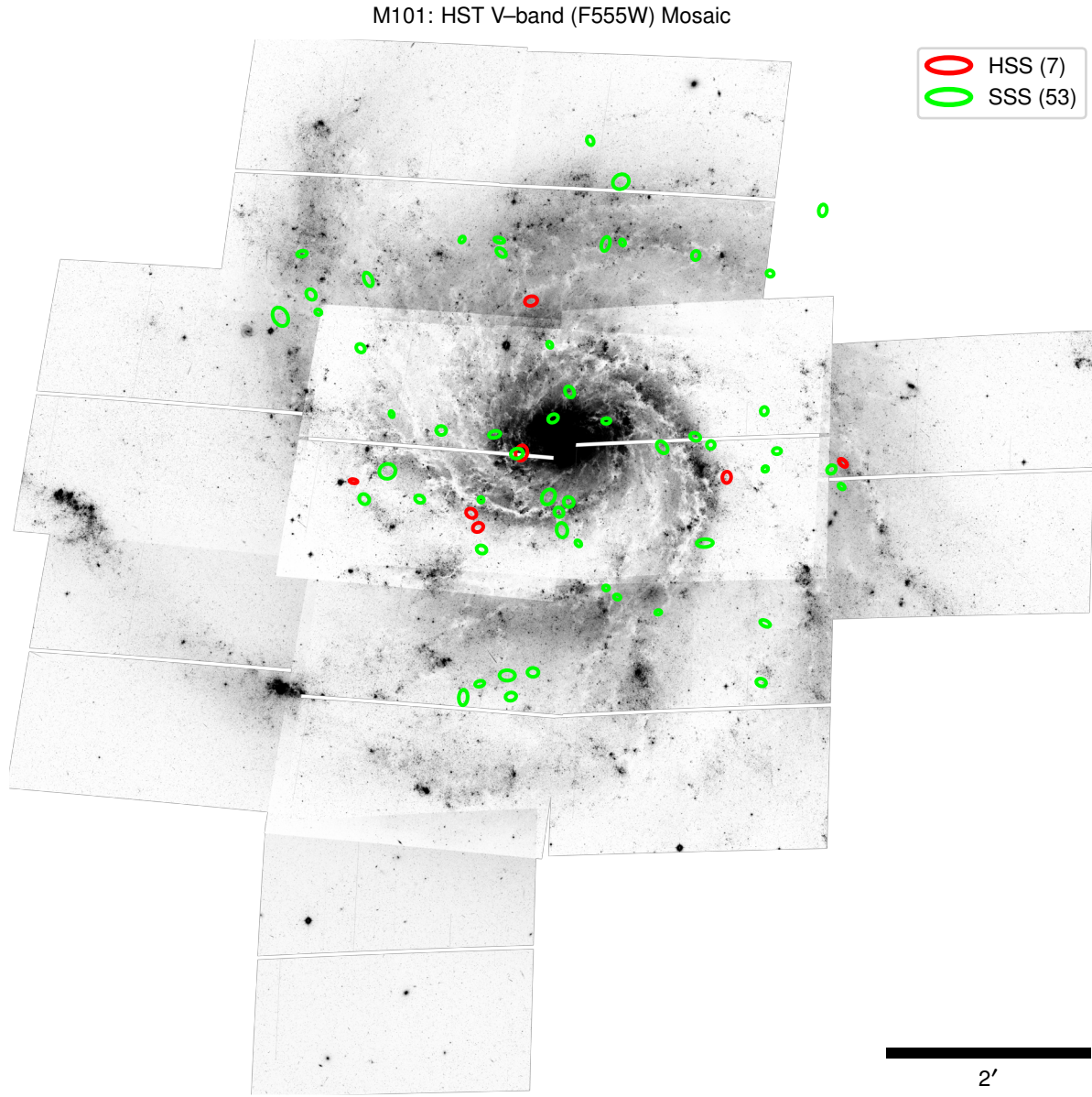


Figure 2 | V-band (F555W) mosaic of 10 Hubble Space Telescope (HST) WFC3 fields in M101. The location of point-like *Chandra* HSSs and SSSs is overlaid. As in Fig. 1, the ellipses represent detections from wavdetect, which considers *Chandra*'s point-spread function's size and orientation at each source location. The figure highlights that both types of X-ray sources primarily appear along the spiral arms of M101. The total number of sources in each category is indicated in parentheses.

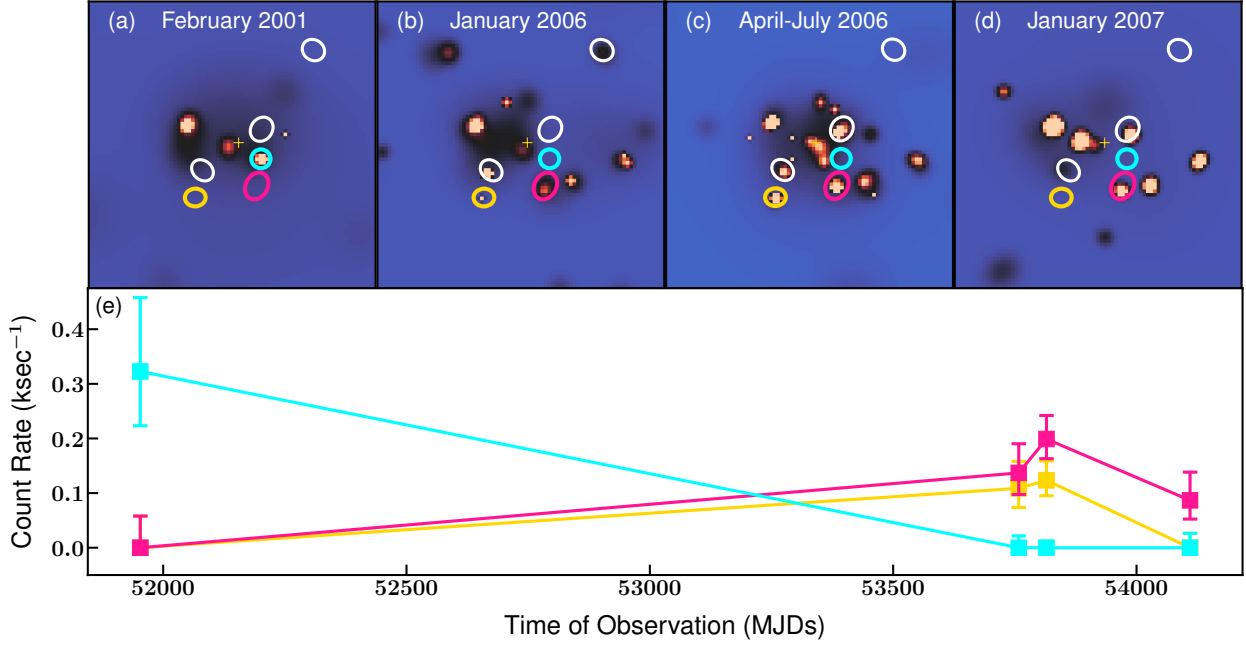


Figure 3 | Time variability analysis of HSSs in NGC 3379. (a-d) 0.15–0.3 keV cutout images ($40'' \times 40''$) showing the central region of the galaxy across four different epochs. The ellipses denote HSSs (with sizes and orientations as described in Fig. 1), while the small "+" sign marks the galaxy's center. (c) combines data from two separate observations in April and July 2006 (total exposure 152 ks); as the HSSs remained relatively steady during this interval, we merged the observations to improve the S/N ratio. One HSS near the center (cyan), detected in 2001, was not observed in the 2006/7 epochs, while most HSSs, such as the magenta source detected in 2006/7, were present in all three 2006/7 epochs but not in 2001 (although we note that the observation from 2001 was only 32 ks). Another interesting HSS is located in the southeast (yellow), which appears to have a UV counterpart associated with a star cluster from the 2009/10 HST observation¹⁶. (e) ACIS-S sensitivity-corrected light-curves of the three highly variable color-coded HSSs from upper panels (see *Methods* for sensitivity correction details). The plots reveal that the HSSs are observed in different observations, separated by one year time scales. The images were adaptively smoothed purely for visual clarity and were not used in HSS detection or light curve generation.

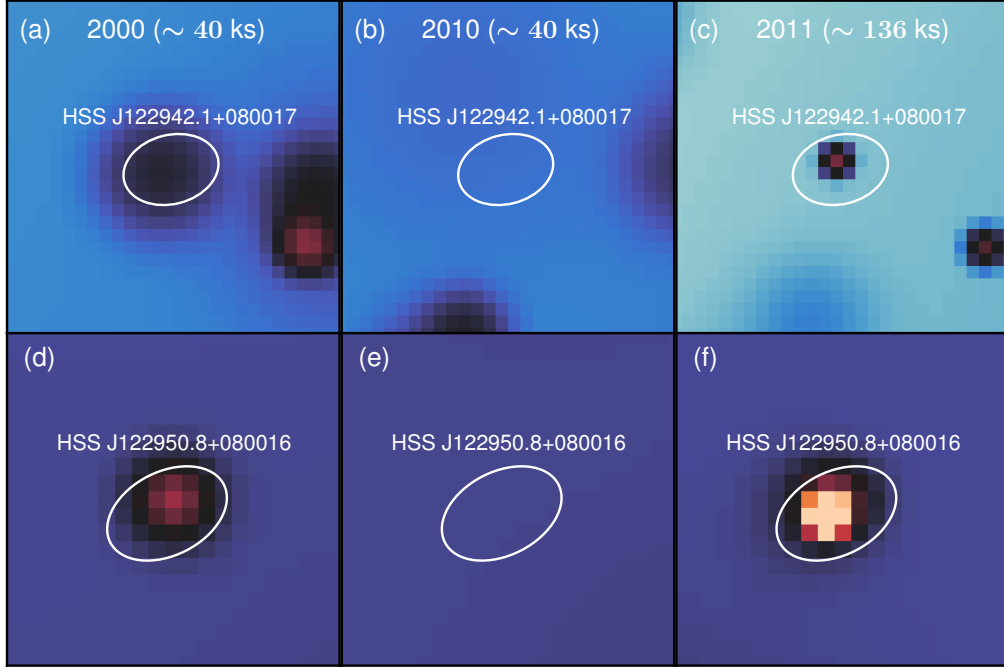


Figure 4 | 0.15–0.3 keV *Chandra* cutout images ($10'' \times 10''$) of NGC 4472 across three different epochs, highlighting two HSSs that display recurrent or potentially persistent behavior. The ellipses represent the PSF size and orientation at each source location from wavdetect. (a–c) HSS J122942.1+080017, located northeast of the galactic center, and (d–f) HSS J122950.8+080016, positioned to the northwest. Both are visible in 2000 (~ 40 ks) and 2011 (~ 136 ks) but absent in 2010. This non-detection in 2010 was attributed to the degradation of *Chandra*'s ACIS-S soft X-ray sensitivity, which necessitates longer exposure times in later years.

Methods

Chandra Observation and Data Reduction

Due to the accumulation of contaminants on *Chandra*'s Advanced CCD Imaging Spectrometer (ACIS) detectors over the years, which absorb soft photon energies, the detection of HSSs through the 0.15–0.3 keV channel has become increasingly difficult in recent years. Therefore, we used archival ACIS-S images and event files of the galaxies listed in Table 1, up to the year 2017 (with justification for this limit provided later). These data were reprocessed and calibrated using CIAO (version 4.16) and CALDB (version 4.11.55), following standard data reduction procedures from the *Chandra* X-ray Center (CXC). This process ensures the correction of charge-transfer inefficiencies and bad pixels and creates a new flare-cleaned level-2 event file for each observation. For each galaxy, we subsequently merged available observations using the script *merge_obs*, which reprojects and combines observations to the same tangent point, creating merged event files and images. The point-spread function (PSF) size for a given image was determined based on the 80% enclosed counts fraction at each pixel location.

Computing ACIS-S's Time-Dependent Sensitivity

To estimate the changes in ACIS-S's sensitivity since its launch, we consider the galaxy cluster Abell 1795, a non-variable cosmic X-ray source, as our master calibrator. We found 18 ACIS-S observations with a total exposure of 238 ks in the archive where the cluster centroid ($\alpha_{J2000.0} = 13^h 48^m 52.70^s$, $\delta_{J2000.0} = +26^\circ 35' 27''$) does not fall off the chip. These observations were reprocessed using a procedure similar to the one previously discussed. For each event file, we created 0.15–0.3 keV and 0.3–1.0 keV threshold images and exposure maps, using

effective energies of 0.2 keV and 0.6 keV, respectively. These threshold images were used to calculate photon counts within a 20'' extraction circle centered on the cluster. Net photon counts were derived after subtracting the background estimated from an annulus (180–220''), where the X-ray surface brightness is <3% of that in the central 20'' and is dominated by residual cluster soft excess, particle, and cosmic X-ray backgrounds. We also calculated the average effective exposure times from the exposure maps by extracting average values from the same circles and normalizing them by the maps' maximum values. Dividing net photon counts by the average effective exposure gives exposure-normalized counts, which we later re-normalized to the first observation time.

In Extended Data Fig. 1, we show these re-normalized counts as a function of observatory age (in modified Julian dates). The figure clearly demonstrates a significant reduction in re-normalized counts in later years, particularly after Cycle 18 (year 2017), where the values drop below 20% of the original counts in Cycle 1 (year 1999) in both the 0.15–0.3 keV (red) and 0.3–1.0 keV bands (lime). Therefore, we set Cycle 18 as our limiting cycle, as discussed earlier, because beyond this point, the detectability of HSS photons becomes extremely challenging.

After considering several models to fit these data, we found that quartic polynomial functions best represent the sensitivity degradation for both bands, with reduced chi-square statistics of $\chi^2_v \approx 0.34$ and $\chi^2_v \approx 1.2$, respectively. These models are shown as dashed red and dotted lime curves in the figure. We later utilized these models in our analysis to account for the degradation of the sensitivity over time.

HSS Identification

To identify HSS candidates in each galaxy, we initially run `wavdetect`²⁹ on the merged 0.15–0.3 keV images, following³⁰. We used wavelet scales of 1, 2, 4, 8, and 16 pixels. A point

source is considered as an HSS candidate when it shows counts below 0.3 keV energy, with a minimum of a 3σ detection above the local background. Additionally, we require no significant detection ($< 3\sigma$) above 0.3 keV. This evaluation is performed over a background area at least five times the size of the region enclosing 80% of the source's PSF. In general, these background extraction regions are circular annuli concentric with the source regions. However, in crowded areas, the background regions were modified to ensure that they did not overlap with any source regions. In contrast, SSS candidates are identified if they are detected in ≤ 1.0 keV but lack any detection signals in higher energy bands.

We performed the same procedure on individual observations to increase our sample completeness, ensuring that we did not miss any source that was detectable in a specific epoch but undetectable in merged observations due to added background noise from additional observations. As an additional classification criterion, we require the 0.15–0.3 keV to 0.3–1.0 keV photon ratio to exceed 8—whether measured in individual or merged observations—for a source to be classified as an HSS (see *Spectral Analysis* for justification). Sources with ratios below this threshold are instead classified as SSSs if they lack detectable emission above 1 keV. To further improve the purity of our sample, we visually inspected each source to eliminate any potential false-positive detections that might originate from the extended structure of the host galaxy or inadequately sampled background regions. With at least 3σ detections above their local background, HSSs are unlikely to be detector artifacts or cosmic-ray afterglows. Their detection in multiple epochs further rules out Poisson fluctuations. Moreover, they cannot be clumps of low S/N hot gas in the galaxies since they are found more readily in nearby hot gas-poor galaxies.

For the brighter HSSs, spectral variations were investigated where the data permitted; consequently, a small fraction ($< 10\%$) of HSSs may exhibit phase transitions. In subsequent

observations, the source appeared to return to its HSS state, indicating a possible phase transition from HSS to SSS and back to HSS. Furthermore, some HSSs in our sample from M31 were previously classified as low-temperature SSSs (with optical nova counterparts) in earlier X-ray studies^{11,17,31}. These classifications were based on detections in the 0.2–1.0 keV bands from XMM-Newton, *Chandra*, and ROSAT observations, although most of their emissions were concentrated in the 0.2–0.3 keV band.

Counterpart Identification

In NGC 3115, we identified an HST counterpart to the highly variable HSS J100514.4–074358 in an ACS/WFC F475W image from March 2012, after registering both datasets to the *Gaia* frame, with a residual relative offset of $\approx 0.31''$. The source was not detected in X-rays prior to February 2012, appeared in the optical in March 2012, and was again undetected in X-rays in April 2012. In M101, HSS J140300.4+541951 lies in a crowded HST WFC3/UVIS F300X field, with at least one UV source within the 1σ X-ray positional uncertainty after registering both images to the *Gaia* frame (offset $\approx 0.29''$). In NGC 3379, HSS J104749.9+123447 appears to have a UV counterpart in HST WFC3/UVIS F225W imaging, consistent with a source reported earlier¹⁶. However, tying the HST image to the *Gaia* frame is challenging due to the paucity of UV sources in the field, preventing a robust astrometric verification. Additional candidate counterparts may be present in M101, NGC 4472, and NGC 4697, and will be investigated in a future study.

Spectral Analysis

Fitting a spectrum and deriving the X-ray luminosity for an HSS is challenging, given the limited calibration data available for the ACIS detectors below 0.3 keV. As a more robust way to obtain fluxes of our HSS candidates, we derived a counts-to-energy conversion factor in the 0.15–0.3 keV range using normal X-ray binaries that emit in both the 0.15–0.3 keV and harder (e.g., 0.5–6.0 keV) bands. For each target galaxy, we extracted the full spectra from these binaries using `specextract` and combined them into a single spectrum to boost photon statistics in the 0.15–0.3 keV band, thereby enhancing the statistical reliability of the analysis. We then fit an absorbed power-law model in the 0.5–6.0 keV range using XSPEC⁴², obtaining a best-fit photon index in the range 1.5–1.8 for six galaxies. The model was extrapolated to estimate the unabsorbed flux in the 0.15–0.3 keV band. By dividing this flux by the total photon counts in the 0.15–0.3 keV range from the combined spectrum and multiplying it by the total exposure time, we derived a 0.15–0.3 keV counts-to-energy flux conversion factor. This factor was then applied to the count rates of HSSs identified in each galaxy to estimate their luminosities in the 0.15–0.3 keV band.

To validate this method, we also fit a thermal *APEC* model in the 0.5–6.0 keV range to the hot gas in NGC 4472, incorporating an additional power-law component for residual X-ray binary contributions within the galaxy. The luminosity estimates obtained using this alternative approach were consistent with those from the power-law model, differing by no more than 25%. This demonstrates that the hypersoft conversion factor is only modestly dependent on the chosen spectral model, given such a narrow energy band (0.15–0.3 keV).

Following the methods discussed above, we derive 0.15–0.3 keV luminosities in the range of $10^{35} - 10^{36}$ erg/s for M31 HSSs, while large elliptical galaxies such as NGC 4472 and NGC 3379 harbor HSSs with luminosities in the range of $10^{36} - 10^{37}$ erg/s, with some even exceeding 10^{38} erg/s. These high luminosities in such a narrow energy band suggest potentially very high

bolometric luminosities, depending on the exact temperatures of the sources. However, the low count rates in this band make it challenging to constrain the temperatures, assuming their blackbody emission peaks in the EUV. Among the known M31 HSSs associated with recent novae, two have temperature estimates of 11 and 17 eV (M31 2001-10a and M31 1996-08b, based on XMM-Newton Observations)^{10,11,43}. As shown in Extended Data Fig. 2, the corresponding bolometric correction factors for these temperatures are 1612 and 44, respectively. In contrast, the SSSs from M31 (according to our classification scheme) have higher temperature estimates, with the lowest being 30 eV (M31 2000-07a)¹¹, corresponding to a bolometric correction factor of only 4.

Additionally, ultraviolet spectroscopy performed with the Cosmic Origins Spectrograph (COS) aboard the HST led to demonstrate that RX J0439.8-6809—a persistent bright SSS identified by ROSAT and located in the Milky Way galactic halo—is likely associated with a hot Milky Way WD with a temperature of 21 eV (250,000 K)⁴⁴. The interstellar hydrogen column density (N_{H}) toward this source is estimated to be $5 \times 10^{20} \text{ cm}^{-2}$ ⁴⁴, which falls within the range of Galactic column density estimates for the HSSs in our sample (Table 1). An early *Chandra* ACIS-S observation revealed that this source has a 0.15–0.3 keV to 0.3–1.0 keV photon ratio of 5.7:1. Summing the 0.15–0.3 keV and 0.3–1.0 keV counts for all the HSSs in NGC4697, NGC3379, and NGC3115 (the cleanest, minimally absorbed galaxies in our sample) yielded 570 ± 32 and 69 ± 27 counts, respectively, for the two bands. This yielded a 0.15–0.3 keV to 0.3–1.0 keV ratio of $8.2 \pm 3.2:1$. Note that, although individual HSSs may not exhibit significant 0.3–1.0 keV emission, the cumulative signal from multiple sources can achieve statistical significance. We therefore adopt a photon ratio threshold of ≈ 8 as an additional criterion for HSS classification. The data indicate that the HSSs in our sample exhibit a mean 0.15–0.3 keV to 0.3–

1.0 keV photon ratio marginally greater than that of RX J0439.8-6809, suggesting that their mean temperature is likely below 20 eV. Therefore, we estimate that HSSs are no hotter than 20 eV based on the lack of their 0.3–1.0 keV emission, with some potentially being considerably cooler (~ 15 eV).

Notably, in such a narrow band, the bolometric correction is strongly dependent on the assumed blackbody temperature (Extended Data Fig. 2). For instance, the bolometric corrections to the 0.15–0.3 keV luminosities for 25 eV, 20 eV, 15 eV, and 10 eV blackbodies are 7, 18, 105, and 4794, respectively (derived from XSPEC BB models; cyan curve in Extended Data Fig. 2b). Consequently, the highly luminous sources in galaxies such as NGC 3379 and NGC 4472 could have bolometric luminosities exceeding 10^{39} erg/s and possibly approaching 10^{40} erg/s, depending on their exact temperatures. This astounding result suggests that the physical origin of these highly luminous, low-temperature HSSs could be fundamentally different from that of M31 HSSs, which are primarily associated with novae. Interestingly, if an HSS has a blackbody temperature below 18 eV, the Rayleigh-Jeans tail of its spectrum could potentially be detected in the FUV (900–2150 Å or 0.0058–0.0138 keV) using the HST.

To place the luminosities of the brightest NGC 4472 HSSs in context, we compare them with the well-studied very soft Galactic source AG Dra¹². The most luminous HSSs in NGC 4472 already reach narrow-band 0.15–0.3 keV X-ray luminosities of $\sim 10^{38}$ erg s⁻¹, an order of magnitude higher than the bolometric luminosity of AG Dra, even without applying a bolometric correction. A study⁴⁵ reports that AG Dra reaches a ROSAT PSPC count rate of ~ 1 ct s⁻¹ at peak. Using PIMMS and assuming a 15 eV blackbody with $N_H = 3.1 \times 10^{20}$ cm⁻², this corresponds to a 0.15–0.3 keV flux of 8.2×10^{-11} erg cm⁻² s⁻¹, or $L_X \sim 2.2 \times 10^{35}$ erg s⁻¹ at a distance of 4.8 kpc. Applying a bolometric correction of ~ 100 for a 15 eV blackbody yields a bolometric luminosity of

$\sim 10^{37}$ erg s $^{-1}$, illustrating that the NGC 4472 HSSs are substantially more luminous than AG Dra even without bolometric corrections.

For the NGC 4472 sources, adopting a nominal effective temperature of 20 eV implies a minimum bolometric correction factor of ~ 18 for a blackbody—the smallest value expected for any reasonable spectral model—while multicolor disk (MCD)⁴⁶ models indicate substantially larger corrections, typically 3–4 times higher (Extended Data Fig. 2b). To account for the low counts of these sources (or any HSSs in other galaxies), uncertainties (1σ) in the measured counts were estimated using a Bayesian approach, which is appropriate for small-number Poisson statistics⁴⁷. In short, for each source, we computed the posterior probability distribution of the true source counts given the observed total counts in the source and background regions, adopting a non-informative prior for the source intensity and accounting for the relative areas and exposures of the two regions⁴⁸. Credible intervals were then derived directly from the posterior distribution. These count posteriors were propagated to a 0.15–0.3 keV X-ray fluxes and luminosities through deterministic transformations using the appropriate energy conversion factors and distances, and uncertainties on derived quantities were obtained by applying the same transformations to the posterior bounds. Consequently, our reported lower limits on the bolometric luminosities ($L_{\text{bol}}(\text{BB})$ column in Extended Data Table 1) are computed using this minimum bolometric correction and the 90% lower credible bound of the 0.15–0.3 keV luminosity (i.e., $L_{\text{X}} - 1.64\sigma$). Even under these conservative assumptions, many sources exceed 1×10^{38} erg s $^{-1}$.

Data Availability: The *Chandra* data supporting the findings of this study are available in the *Chandra* Data Archive under the identifier doi:[10.25574/cdc.395](https://doi.org/10.25574/cdc.395).

Code Availability: The code used to generate catalogs, figures, and relevant results in this study are additionally accessible from Zenodo: doi: [10.5281/zenodo.18399475](https://doi.org/10.5281/zenodo.18399475)

References

29. Evans, I. N. *et al.* The Chandra Source Catalog Release 2 Series. *Astrophys. J.S.* **274**, 22 (2024).
30. Brastad, N. J. *et al.* Deep Chandra Monitoring Observations of NGC 3379: Catalog of Source Properties. *Astrophys. J.S.* **179**, 142 (2008).
31. Makarov, D., Prugniel, P., Terekhova, N., Courtois, H. & Vauglin, I. HyperLEDA. III. The catalogue of extragalactic distances. *Astron. Astrophys.* **570**, A13 (2014).
32. Riess, A. G., Fliri, J. & Valls-Gabaud, D. CEPHEID PERIOD–LUMINOSITY RELATIONS IN THE NEAR-INFRARED AND THE DISTANCE TO M31 FROM THE HUBBLE SPACE TELESCOPE WIDE FIELD CAMERA 3. *Astrophys. J.* **745**, 156 (2012).
33. Beaton, R. L. *et al.* The Carnegie-Chicago Hubble Program. VII. The Distance to M101 via the Optical Tip of the Red Giant Branch Method. *Astrophys. J.* **885**, 141 (2019).
34. Tonry, J. L. *et al.* The SBF Survey of Galaxy Distances. IV. SBF Magnitudes, Colors, and Distances. *Astrophys. J.* **546**, 681 (2001).
35. Brastad, N. J. *et al.* THE SPECTRAL AND TEMPORAL PROPERTIES OF TRANSIENT SOURCES IN EARLY-TYPE GALAXIES. *Astrophys. J.* **755**, 162 (2012).
36. Cappellari, M. *et al.* The ATLAS3D project – I. A volume-limited sample of 260 nearby early-type galaxies: science goals and selection criteria. *Mon. Not. R. Astron. Soc.* **413**, 813–836 (2011).

37. Blakeslee, J. P. *et al.* THE ACS FORNAX CLUSTER SURVEY. V. MEASUREMENT AND RECALIBRATION OF SURFACE BRIGHTNESS FLUCTUATIONS AND A PRECISE VALUE OF THE FORNAX–VIRGO RELATIVE DISTANCE. *Astrophys. J.* **694**, 556 (2009).

38. Dickey, J. M. & Lockman, F. J. H I in the galaxy. *Annu. Rev. Astron. Astrophys.* **28**, 215–261 (1990).

39. Freeman, P. E., Kashyap, V., Rosner, R. & Lamb, D. Q. A Wavelet-Based Algorithm for the Spatial Analysis of Poisson Data. *Astrophys. J.S.* **138**, 185 (2002).

40. Vikhlinin, A. *et al.* Evolution of Cluster X-Ray Luminosities and Radii: Results from the 160 Square Degree ROSAT Survey. *Astrophys. J.* **498**, L21 (1998).

41. Pietsch, W. *et al.* X-ray monitoring of optical novae in M 31 from July 2004 to February 2005. *Astrophys. J.* **465**, 375–392 (2007).

42. Arnaud, K. A. XSPEC: The First Ten Years. In *Astronomical Data Analysis Software and Systems V* (eds. Jacoby, G. H. & Barnes, J.) *ASP Conf. Ser.* **101**, 17 (1996).

43. Henze, M. *et al.* X-ray monitoring of classical novae in the central region of M 31. I. June 2006–March 2007. *Astron. Astrophys.* **523**, A89 (2010).

44. Werner, K. & Rauch, T. Analysis of HST/COS spectra of the bare C–O stellar core H1504+65 and a high-velocity twin in the Galactic halo. *Astron. Astrophys.* **584**, A19 (2015).

45. Greiner, J. *et al.* UV and X-Ray Monitoring of AG Draconis During the 1994/1995 Outbursts. in *Supersoft X-Ray Sources* vol. 472 267 (1996).

46. Mitsuda, K. *et al.* Energy spectra of low-mass binary X-ray sources observed from Tenma. *Publications of the Astronomical Society of Japan* **36**, 741–759 (1984).

47. Kraft, R. P., Burrows, D. N. & Nousek, J. A. Determination of Confidence Limits for Experiments with Low Numbers of Counts. *Astrophys. J.* **374**, 344 (1991).
48. Park, T. *et al.* Bayesian Estimation of Hardness Ratios: Modeling and Computations. *Astrophys. J.* **652**, 610–628 (2006).

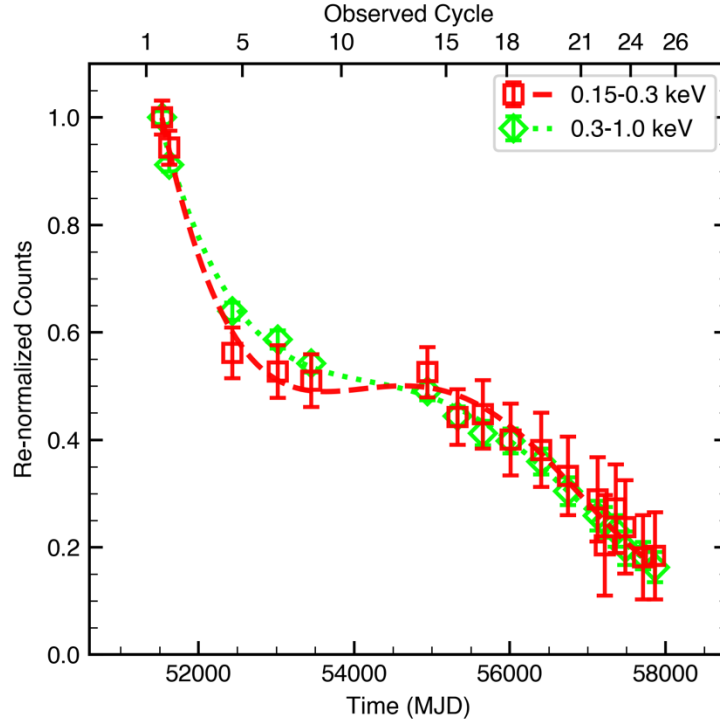
Acknowledgments: This scientific work uses data obtained from archival *Chandra* X-ray Center observations, which is operated by the Smithsonian Astrophysical Observatory for and on behalf of NASA under contract NAS8-03060. This work was supported by the *Chandra* X-ray Center under grant AR4-25004X (M.M., J.A.I.). R.D.S. would like to acknowledge support from NSF AST-2009520.

Author Contributions: J.A.I., M.M., and R.D.S. jointly conceived the project. M.M. and J.A.I. developed the methodology. The investigation was carried out by M.M., J.A.I., and R.D.S. Data visualization was performed by M.M., J.A.I., and R.D.S. M.M. and J.A.I. secured *Chandra* funding for the project. Project administration was handled by J.A.I. and M.M., with supervision provided by J.A.I., R.D.S., and M.M. The original manuscript draft was written by M.M., R.D.S., and J.A.I., and all authors contributed to reviewing and editing the final version.

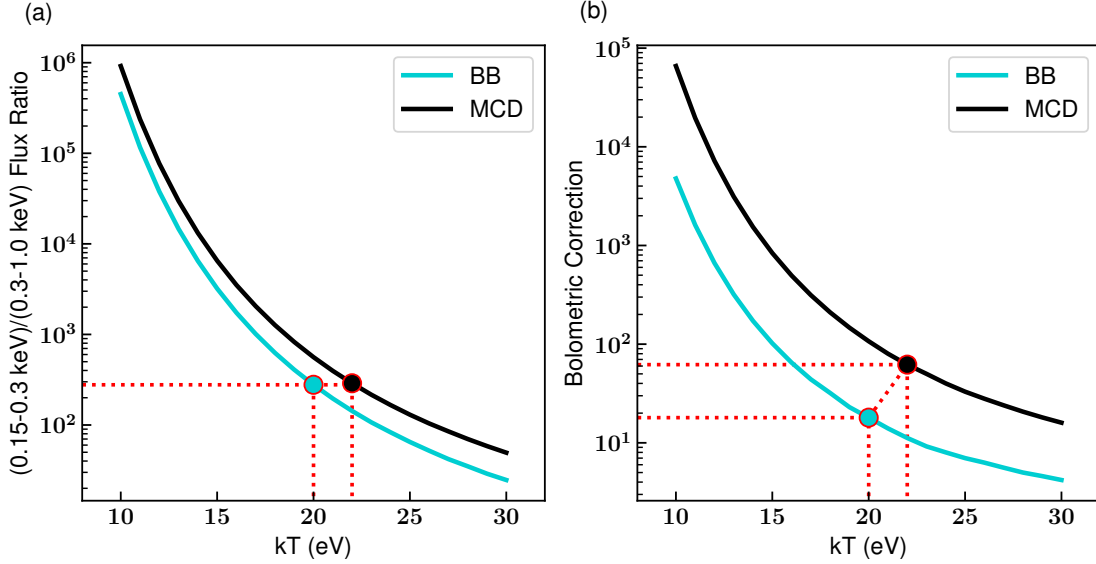
Competing Interests: The authors declare that they have no competing financial interests.

Correspondence: Correspondence and requests for materials should be addressed to M.M. (mmuhibullah@crimson.ua.edu).

Extended Data



Extended Data Figure 1: Exposure re-normalized number counts in the 0.15–0.3 keV and 0.3–1.0 keV bands, estimated from Abell 1795 as a function of Modified Julian Date (MJD) and *Chandra* observing cycle. The plot illustrates the progressive decline in *Chandra*'s sensitivity over time, particularly in the softest energy channels. The error bars represent 1σ uncertainties. The dashed red curve and dotted lime curve correspond to the best-fit quartic polynomial models with $\chi^2 \approx 0.34$ and $\chi^2 \approx 1.2$, respectively. Interestingly, the ratio of 0.15–0.3 keV to 0.3–1.0 keV counts remains relatively consistent over time.



Extended Data Figure 2: Model-predicted flux ratios and bolometric corrections vs. source temperature. (a) The 0.15–0.3 keV to 0.3–1.0 keV flux ratio for the thermal blackbody (BB) and multicolor disk (MCD) models, respectively. The horizontal dashed red line indicates the flux ratio at which HSSs are expected to be hottest ($kT_{BB} \approx 20$ eV), corresponding to a slightly higher temperature for the accretion disk model ($kT_{MCD} \approx 22$ eV). (b) shows that the bolometric correction for the MCD model is approximately 3–4 times higher than that of the BB model at the respective temperatures.

Extended Data Table 1 | Properties of HSSs discovered in this work.

A portion of the full catalogue is shown here for guidance regarding its form and content. The complete table is provided as Supplementary Data Table 1, and a machine-readable version is available at https://zenodo.org/records/18399475/files/ed_table1.fits?download=1

Galaxy	Distance (Mpc)	Object	Good Exp. (ks)	RA (J2000)	Dec (J2000)	Counts (0.15-0.3kev)	Counts Err.	Area (arcsec ²)	Bg. Counts (0.15-0.3kev)	Bg. Err.	Bg. Area (arcsec ²)	L _X (0.15-0.3keV) (erg/s)	L _{bol} (BB) (erg/s)	L _{bol} (MCD) (erg/s)	Counter parts	SSS Phase
M31	0.8	HSS J00424 8.7+41 1626	369.5	00:42:48 .70	+41:16:26 .49	51	7.52, - 6.78	2.66	28.0	5.66, - 5.03	84.72	1.54E36	2.21E37	7.60E37	Nova (Pietsch+, 2007; Hofmann +, 2013)	ObsIDs: 13826 (2.6 σ), 14197 (2.4 σ)
M101	6.5	HSS J14032 1.7+54 2024	1057.0	14:03:21 .71	+54:20:23 .54	105.0	10.63, - 9.94	11.86	100.0	10.24, -9.64	193.17	6.52E37	9.90E38	3.41E39	SSS (Liu, 2011; Wang+, 2016)	ObsIDs: 5338 (2.9 σ), 6114 (2.1 σ)
NGC3115	9.7	HSS J10051 2.8- 074117	1138.7	10:05:12 .81	07:41:17. 45	30.0	5.84, - 5.12	13.56	315.0	18.05, -17.45	2037.45	3.54E37	4.66E38	1.61E39	SSS (Wang+, 2016)	-
NGC3379	10.6	HSS J10474 9.3+12 3456	337.1	10:47:49 .31	+12:34:56 .27	41.0	6.84, - 6.01	6.54	39.0	6.59, - 5.95	85.69	5.90E37	8.08E38	2.78E39	SSS (Wang+, 2016)	ObsID: 7074 (1.95 σ)
NGC4697	11.4	HSS J12483 7.6- 054811	193.0	12:48:37 .59	05:48:11. 15	12.0	3.89, - 3.2	8.71	4.0	2.46, - 1.82	105.54	2.01E37	2.25E38	7.75E38	-	-
NGC4472	16.7	HSS J12293 8.7+08 0239	229.7	12:29:38 .73	+08:02:39 .48	12.0	3.86, - 3.19	30.26	27.0	5.58, - 4.95	511.24	1.09E38	1.14E39	3.92E39	-	-

Notes: (i) Asymmetric (upper and lower) uncertainties (1 σ) in counts (Counts Err. and Bg. Err.) are estimated from the Bayesian posterior probability distribution^{47,48}. (ii) Lower limits on the bolometric luminosities for both the blackbody (L_{bol}(BB)) and multicolor disk blackbody (L_{bol}(MCD)) models are derived using a minimum bolometric correction factor of 18 and the 90% lower credible limit of the 0.15–0.3 keV luminosity (i.e., L_X – 1.64 σ). (iii) Counterparts indicates matched X-ray coordinates from the literature. (iv) SSS Phase indicates observations in which the HSS exhibited a supersoft spectral state, including the detection significance for that state.